

Parallel coupling of trapped ions in multiple individual wells

A. Podlesnyy,^{1,2} Y. Suleimen,^{1,2,*} L. A. Akopyan,² and K. Lakhmanskii²

¹*Moscow Institute of Physics and Technology, Moscow region 141701*

²*National Quantum Laboratory, Skolkovo, Moscow 143025*

In this paper we offer a new surface trap design capable of coupling the ion motion in the selected wells among ten by adjusting the DC-voltages on a set of electrodes. We demonstrate and characterize a variety of phonon mode spectra for different voltage sets for 10 ion-architecture for two types of ions Ca and Be. We found that it is possible to unite the ions into segments with unique phonon mode frequencies to perform parallel MS-gate operations. We also model the fidelity of the MS-gate operation for a segment comprise of two ions accounting the two main contributions to the gate infidelity: the limited frequency difference between phonon frequencies of the segments and the finite drift of the phonon frequencies expected in experiment. Additionally, we investigate how the number of ions per individual trap and an anharmonic potential terms affect the coupling between the two wells.

I. INTRODUCTION

Since Cirac and Zoller proposed an implementation of quantum computer(QC) using individual atomic ions [1], trapped ions have remained one of the leading technology platforms for large-scale QC. In particular, few-ion-qubit systems have successfully demonstrated and fulfilled all of DiVincenzo's original criteria [2] with high fidelity [3, 4]. However, practical realizations of QC require the ability to increase the number of simultaneously trapped ions while maintaining the ability to control and measure them individually with high fidelity [5]. Single linear arrays of ions encounter significant limitations in that respect. This is primarily due to the fact that the speed and performance of two-qubit gates between ions in a chain generally decreases as the total number of ions grows [6]. A promising approach around these issues is to break a single long ion chain into segments [1, 7]. Each such a segment or module can trap a restricted number of ions to maintain high fidelity and high-speed operations. In such a modular approach, each subsystem can be built and tested independently, has a particular and well-defined functionality, and is compatible with the other subsystems. Therefore 2D arrays of traps have the potential to offer a faster and higher-fidelity method to distribute quantum information over a many-ion array [8–10].

The challenge, then, becomes how to move quantum information between the modules. The coupling between the ions in separated segments can be achieved in different ways: through transport [7], through effective spin-spin interactions [1], shared electrically floating electrode [11, 12] or controlled orientation of the circular modes [13]. Here we focus on the alternative method: the exchange of the phonons between separate wells. Proof-of-principle investigations [14–16] demonstrated its efficiency for two trapping regions. In this paper we offer a new surface trap design capable of coupling the ion

motion in the selected wells among ten by adjusting the DC-voltages on a set of electrodes. We demonstrate and characterize a variety of phonon mode spectra for different voltage sets for 10 ion-architecture for two types of ions Ca and Be. We found that it is possible to unite the ions into segments with unique phonon mode frequencies to perform parallel MS-gate operations. We also model the fidelity of the MS-gate operation for a segment comprise of two ions accounting the two main contributions to the gate infidelity: the limited frequency difference between phonon frequencies of the segments and the finite drift of the phonon frequencies expected in experiment. Additionally, we investigate how the number of ions per individual trap and an anharmonic potential terms affect the coupling between the two wells.

II. TRAP STRUCTURE

The connection or coupling between trapped ions is achieved through their strong coulomb interaction [1, 7]. Only the ions sharing the same phonon mode of motion can be efficiently entangled. In this section we present a novel trap design, developed for the selective manipulation of the phonon mode spectrum of an ion crystal with an electrode voltage set.

A key to control normal modes of an ion crystal lies in precise tuning of pseudopotential hessian $(A_{in})_k$ [17]. It can be represented as:

$$(A_{ij})_k = \delta_{ij} m_i (\omega_i^2 / 2)_k + (C_{ij})_k, \quad (1)$$

where C_{ij} is a Coulomb interaction hessian, δ_{ij} – Kronecker delta, m_i – mass of ion i , ω_i – secular frequency of single ion in a trap i and k denotes principal axis of oscillations along x, y, z . The normal modes of oscillation $Q_m(t) = \sum_{m=1}^N b_{im} q_i(t)$ are derived by diagonalizing A_{ij} , where b_{im} is a normal mode transformation matrix-element between ion i and normal mode m and $q_i(t)$ is the deviation of the coordinate of the ion i from the equilibrium position. The interaction matrix element M_{im} , describing a coupling between ion

* e.suleimen@rqc.ru

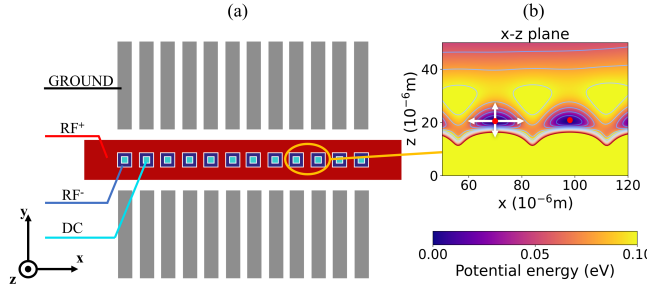


FIG. 1. (a) A surface ion trap geometry, used for simulations in the paper. The trap forms 12 distinct trapping potential wells. Ion confinement with predetermined height is achieved by the single red RF^+ electrode and 12 dark-blue RF electrodes with π phase delay. 12 light-blue DC electrodes in the middle of squares are utilized for secular frequency optimization. The side DC electrodes, depicted in gray, are essential for stray field compensation. (b) Potential distribution above two individual traps. This design has a trap depth of 60-100 meV in the authorized DC voltage range. The principal axes of oscillation are illustrated by white arrows.

i and mode m is represented by a rescaled matrix of normal vectors $b_{im}/\max(b_{im})$. Secular frequencies of each trapping site are computed by diagonalizing the Hessian of the corresponding confining fields as $\omega_i^2 = em_i^{-1}Eig(\partial^2\Psi/\partial r_n\partial r_m)$, for a trap electrodes potential Ψ [18] with e being the elementary charge. The variation of secular frequency may be achieved in an array of individual planar traps by tuning the DC electrode voltages. From the practical point of view in planar traps it's more convenient to change DC voltages, then an RF drive.

Therefore we suggest the structure combining individual and linear surface traps schematically shown in Figure 1 (a). It includes a single RF^+ electrode with 12 square notches, creating separate potential wells. Each notch is filled with an RF^- electrode with the phase delay π used to increase the ion height above the surface and a central optimization DC electrode. On the both sides of an RF^+ electrode 12 side DC electrodes are presented (labeled "ground" in Fig. 1 (a)). The side DC electrodes may be used for stray fields compensation [19] and for additional tuning of secular frequencies. The trap can confine ions in 10 central wells, while the two residual sites are used for an additional secular frequency optimization. The width of the DC electrodes itself varies from 6 to 12 μm , which restricts the width of the gaps between them to 2 μm .

Figure 1 (b) demonstrates the simulated pseudopotential above the two individual traps. To achieve a global trap depth of about 100 meV we optimize the geometry of the surface trap and RF parameters. The optimum confinement potential for a single $^{40}\text{Ca}^+$ ($^9\text{Be}^+$) ion in a separate well is achieved at $V_{RF} = 80(85)$ V (from 0 to Peak) and at $\Omega_{RF} = 2\pi \times 110(240)$ MHz for both RF^\pm . The ion trapping occurs at the height of 20 μm in each site. The distance of $d_{ion} = 28 \mu\text{m}$ between the individual

potential minima has been demonstrated to be sufficient to share motional quanta over the possible decoherence [14].

RF drive frequencies and voltages have a strong effect on a number of parameters. The potential depth between two neighboring traps in pseudo-potential approximation is $U_{depth} \propto \omega_x^2 d_{ion}^2$. Therefore, high secular frequencies are required while miniaturization to preserve sufficient trap depth. On the other hand, stability parameter for surface ion traps scales proportionally with ω_x : $q \propto \omega_x \Omega_{RF}^{-2}$ and must not exceed 0.908 for the stable motion [20]. From the experimental side the magnitude of V_{RF} is limited which restricts the trapping potential depth as $U_{depth} \propto V_{RF}^2/\Omega_{RF}^2$. This, in general, leads to a shallow depth in chip-based ion traps. The presented optimal Ω_{RF} for preserving stable ion motion and sufficiently low V_{RF} are derived in account to those features.

For the grounded DC electrodes we obtained the following secular frequencies for Be and Ca ions in the central potential well: $(\omega_x, \omega_y, \omega_z)_{Be^+} = (22.60, 38.74, 61.33)$ MHz and $(\omega_x, \omega_y, \omega_z)_{Ca^+} = (10.44, 17.9, 28.34)$ MHz. Such high frequencies allow to reduce heating rate, which scales as $d\langle n \rangle/dt \propto \omega^\alpha$ with $-2 \leq \alpha \leq -1$ [21]. Adopting radial motional modes instead of axial may be beneficial, due to higher secular frequencies. However, the interaction strength Ω_I between the ions in separate wells decreases with higher secular frequencies as described in [16]:

$$\Omega_I^{ij} = \frac{e^2}{4\pi\epsilon_0\sqrt{m_i m_j}\sqrt{\omega_i \omega_j} d_{ion}^3}, \quad (2)$$

where ϵ_0 is the vacuum electric permittivity, $\omega_{i,j}$ are uncoupled secular frequencies, $m_{i,j}$ are the masses of ions, respectively. The coupling strength between ions depends on the geometry, secular frequencies in trapping sites and ion masses. An optimal configuration is presented, which must also obey technical constraints of the system and ensure sufficient trap depth U_{depth} .

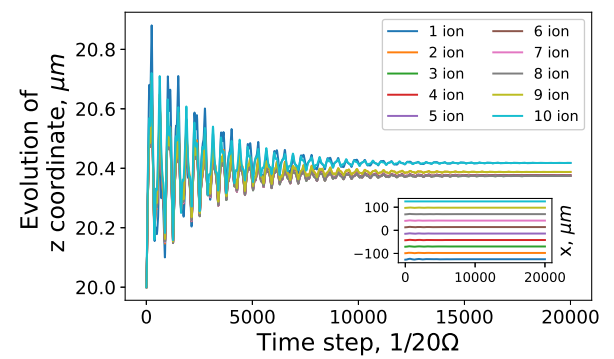


FIG. 2. An evolution of x and z coordinates of 10 trapped ions simulated with grounded DC electrodes and laser cooling. Time step is chosen to be $1/20\Omega_{RF}$. The equilibrium positions of the ions are derived from the simulation. The simulation shows variation in ion heights of magnitude $1.5 \times 10^{-3} z_{\text{mean}}$.

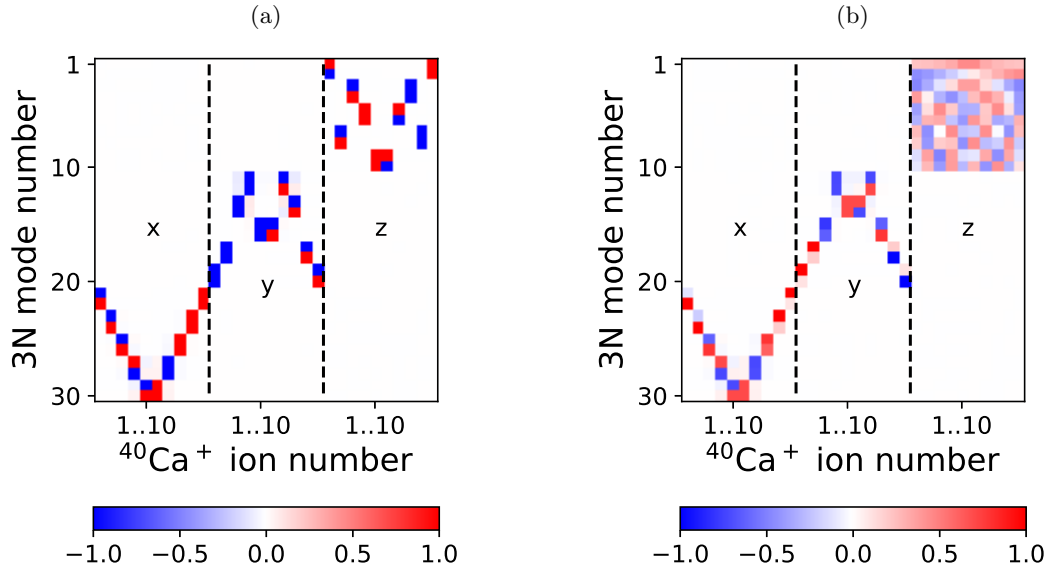


FIG. 3. (a) A normal modes interaction matrix of the ion crystal with grounded DC electrodes from figure 2. The matrix is divided into three parts, representing modes, corresponding to the respective principal axis of oscillation. The cell's color represents the normalized interaction strength between the corresponding ion and normal mode. The difference in secular frequency for z ranges from 0.02 to 0.14 MHz. The matrix represents off-resonance detuning of ion motion without additional voltage optimization. (b) The interaction matrix with applied DC voltage set, optimized for tuning ions in the resonance on the radial secular frequency ω_z (see Figure 4a-b).

The maximization of coupling strength may be described as follows. For the fixed U_{depth} , the secular frequency $\omega_{sec} \propto d_{ion}^{-1}$. An ion-ion coupling strength (2) then $\Omega_I \propto m^{-1} d_{ion}^{-2}$. This shows that for the preserved trap depth the increase of coupling between single ions can be achieved only by lowering the inter-ion distance and ion masses.

Under the presence of a typical parasitic field in the range of 20–30 Vm^{-1} in surface ion traps an electrical barrier 60–70 meV for ion separation should be resistant to dual to solitary trapping site rearrangement [22]. The potential well's depth tends to decrease as more voltage is supplied to the DC electrodes. We identified the operating voltage range on the DC central electrodes in the trapping sites that keeps the trap depth U_{depth} above 50 meV. The voltages in the range between 0 V and 6 V maintain a ratio between the energy of the background gas molecules in the vacuum chamber at room temperature $U_{bcg} \propto 40$ meV and the trap depth below 0.8. In operating regime, the trapped ion's lifespan $\tau = \frac{kT_{300K} \ln(2)}{P\sigma} \sqrt{\frac{\pi m_{H_2}}{8kT_{300K}}} \propto 36 \text{ min}$ [23] in ultra-high vacuum should be adequate to execute quantum processes. Additionally, the influence on the level of the potential barrier between neighboring traps is taken into consideration while setting the limiting voltages on the DC electrodes. Note that the voltages on side and edge DC electrodes are allowed to exceed 6 V, which keeps the trap depth above the threshold.

The complex structure of potential distribution in-

duced by planar traps prevents efficient analytical description of ion motion [24]. Instead, a numerical simulation of ion motion in the trap, considering a time-dependent anharmonic potential, is performed. The simulation allows to obtain equilibrium ion positions \mathbf{x}^o , necessary for normal mode derivation [25]. The details on simulation are described in Appendix A in detail.

Simulation of trapped-ion dynamics for the 0 DC voltage case, represented by the evolution of the ions x and z coordinates is presented in Figure 2. The simulation results represent a small variation in equilibrium ion heights. This non-linearity in the ion crystal could potentially lead to the coupling of normal modes corresponding to different principal axes. Therefore, the calculation of the normal modes in all three coordinates is performed.

III. SPECTRAL SEGMENTATION

Here we demonstrate that the proposed surface trap design allows to unite or separate phonon mode frequencies of the selected ions. For this we optimize the voltages on the central DC electrodes.

As a first step we compute the phonon mode frequencies for the configuration where all central DC electrodes are grounded with the results shown in Figure 3a. As can be seen, there is no interaction of motional modes along the different principal axes. Therefore the considered ion crystals can be interpreted as linear ion chains. Indeed our simulation of the ion trajectories confirm this

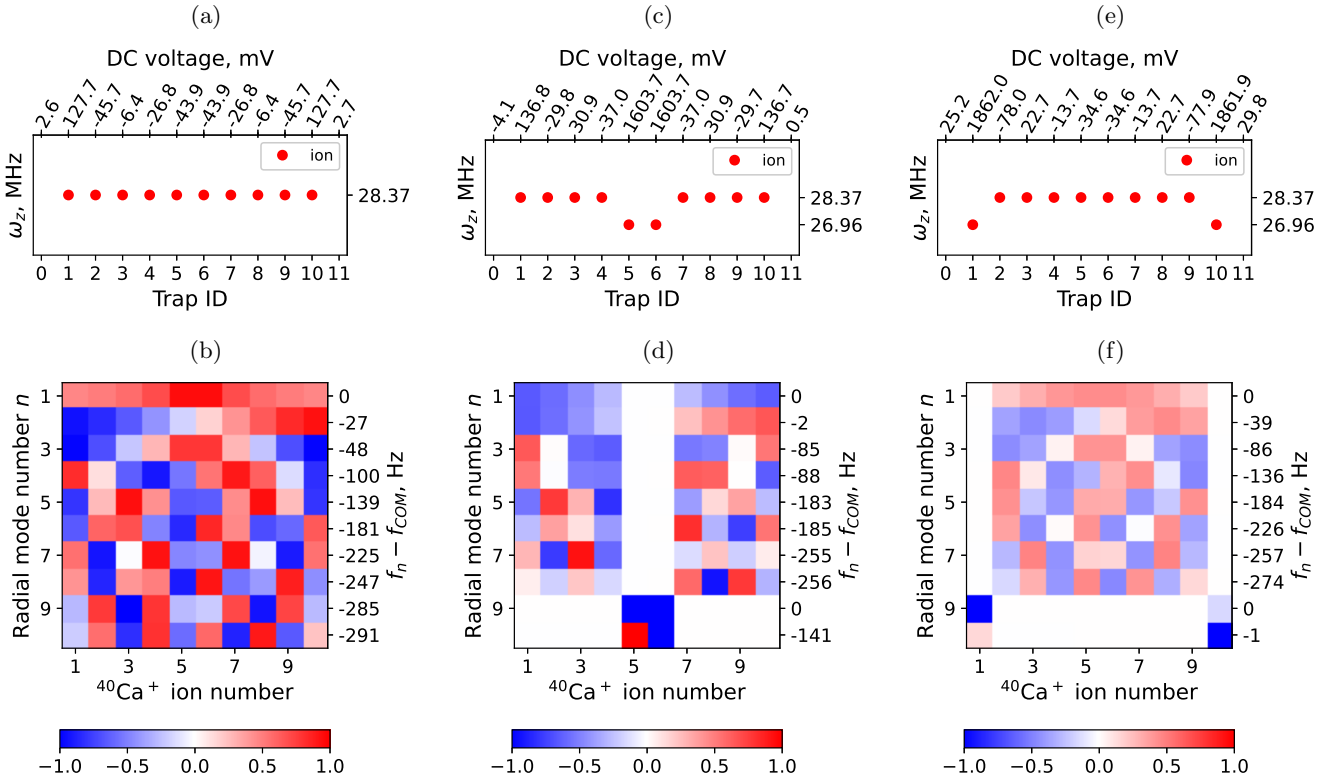


FIG. 4. Phonon spectrum of 10 $^{40}\text{Ca}^+$ ion crystals in different DC voltage set configurations. (a-c) A secular frequency spectrum of single ions depending on the trap ID. The top x axis shows required DC voltages on the central electrodes. The 0 and 11 traps are used as endcap voltages to decrease the required voltage in trapping sites, and does not contain ions. (b) Radial normal mode interaction matrix for the voltage structure from Figure 3b. The right y axis represents frequency shifts of normal modes from the COM mode, equal to the secular frequency from (a). (d) Interaction matrix for the voltage configuration with two pinned central ions. The right y axis represents frequency shifts from COM modes for two different phonon spectra segments, depicted on (c) – pinned central ions and the rest. (f) Interaction matrix for ion crystal for two pinned edge ions.

as shown in figure 2: the difference in ion heights is significantly lower than the variation in ion crystal length. On the other hand, the pairs of ions $(i, 11 - i)$, $i = \overline{1, 5}$ form a coupled system sharing the same axial and radial phonon modes independently of the rest of the ions. This is due to the symmetric structure of RF $^\pm$ and DC electrodes forming the following set of secular frequencies: $\omega_i = \omega_{11-i}$ for $i = \overline{1, 5}$. The phonon mode frequency differences between coupled pairs range between 0.02 and 0.14 MHz. For the further discussion it is useful to determine resonance condition:

$$2\Delta_{-}^{i,j} = \omega_i - \omega_j = 0. \quad (3)$$

The connectivity between uncoupled ions is absent because of significant secular frequency difference $|\Delta_{-}^{i,j}| \gg \Omega_I$ [14].

Optimization of the voltages on the central DC electrodes allows to achieve the all-to-all connectivity between ions through modes corresponding to z principal axis as shown in figure 3b.

The symmetrical pattern of the interaction along the x and y axes is preserved, with rearranged orders of the

modes interacting with ion pairs 3, 8 and 5, 6 along the y principal axis.

The optimal DC voltages for different configurations were obtained with an optimization procedure described in Appendix B. The obtained values are shown in Figure 4(a, c, e) together with the secular frequencies in each individual trap, while Fig. 4 (b, d, f) shows the corresponding phonon mode configurations along the principal z axis. Figure 4a-b demonstrates the same configuration as in Figure 3b. Due to the nonlinear nature of the ion crystal and long ion-ion distances, the coupling strength between ions and center-of-mass (COM) mode varies with the ion number. This variation can be minimized by further reducing the difference in the secular frequencies of the ions.

To maintain sufficient ion height we had to use a large distance d_{ion} between the trap wells. As a result, the interaction strength $\Omega_I \propto 1/d_{ion}^3$ [14] and consequently the normal mode frequencies separation $\Delta f = \Omega_I/2\pi$ are low for this trap geometry. Namely, for $^{40}\text{Ca}^+$ ion crystal in configuration from Figure 3b the mean separation of the normal mode frequencies in z direction is 32 Hz. In

ion segments, containing less ions, such frequency separation and hence coupling strength will be higher. An arbitrary configuration of spectral segments can be obtained in our trap. The variation of ion heights z_i with applied voltages does not exceed $1.5 \times 10^{-2} z_{mean}$.

The segmented two central ions configuration is depicted in Figure 4c-d. The spectrally divided segment consists of the modes with indexes denoted $m_{pin} = 9, 10$. The ions are separated on two segments: pinned ions with indexes denoted $i_{pin} = 5, 6$ and the rest ions with indexes denoted $i_{rest} = 1..4, 7..10$. The coupling strength

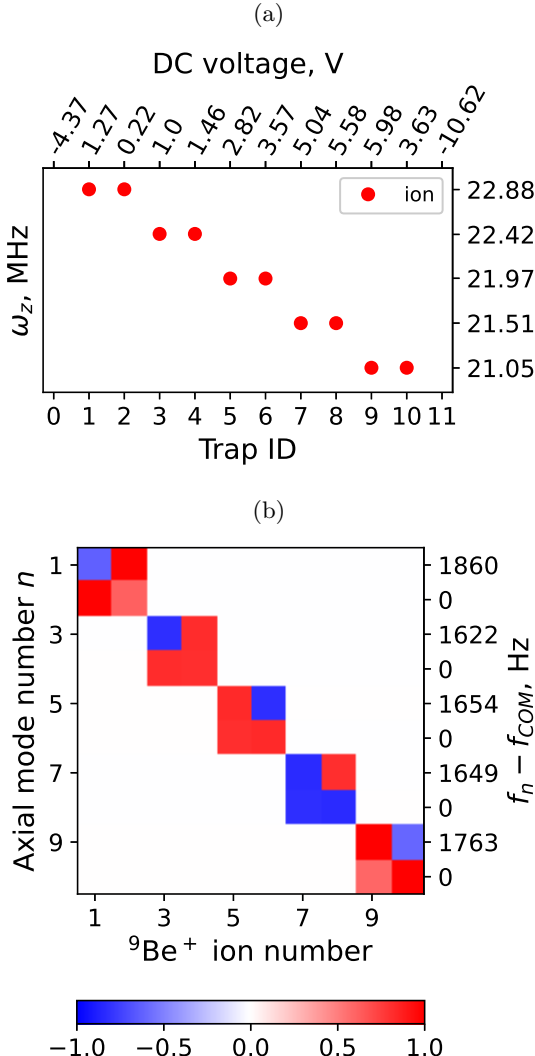


FIG. 5. (a) A secular frequency spectrum of single ions depending on the trap ID. The top x axis shows required DC voltages on the central electrodes. The 0 and 11 traps are used as endcap voltages to decrease the required voltage in trapping sites. (b) A normal mode interaction matrix of ${}^9\text{Be}^+$ ion crystal in the presented voltage set configuration. The right y axis represents the difference between COM modes (0) and stretch mode of each ion pair. The mean frequency separation $\Delta f = 1.7$ kHz.

for pinned ions and the rest to the particular pinning mode satisfies the following relation:

$$\frac{b_{i_{rest}, m_{pin}}}{b_{i_{pin}, m_{pin}}} \leq 10^{-4}, \quad (4)$$

which allows us to consider pinned ion pairs independently.

Longer distances between non-neighboring traps further reduce the interaction between ions. In Figure 4f the interaction matrix of ion configuration with 2 edge ions being pinned is demonstrated. Although the coupling of pinned ions to their modes is preserved, the interaction strength between them is $\Omega_I = 2\pi \times 1$ Hz. In comparison to neighboring ions, the coupling between 2 ions separated by another trap is typically 8 times less. This implies that the two-qubit gates should be performed with neighboring ions for better performance.

The frequency separation $\Delta f \propto \omega_{sec}^{-1} m^{-1}$ is improved further by using Be ions on axial modes, as axial secular frequencies are 73% lower than radial z frequencies. The highest frequency separation of the segmented two Be ions in the axial mode is $\Delta f = 1.8$ kHz. The modes of the ion chain are effectively segregated in this design, allowing for parallel processes. Any n -ion sub-register may execute independent n -qubit quantum operations. The configuration of ions with phonon spectrum, allowing for five parallel two-qubit gates is demonstrated in Figure 5. The ${}^9\text{Be}^+$ ion crystal is separated into five pairs forming parallel spectral segments.

With the additional use of side DC electrodes (Figure 1) for voltage optimization, the phonon spectrum of an ion crystal can be controlled in parallel for all orthogonal principal oscillation axes. The Figure 6 serves as an illustration of the capacity of spectral control in the trap. In this configuration, the interaction between ions is limited only by their neighbors. This is achieved by simultaneous segmentation of radial y and radial z normal mode spectrum on pairs. The ion pairs on each radial principal axes are separated from the rest. For each pair of neighboring ions ($i, i+1$), there exist two modes (COM and stretch) which involve only these two ions. For the pairs ($2i, 2i+1$), these modes are in y direction, whereas for the pairs ($2i+1, 2i+2$) they are in z direction. Still, all ions interact on the primary vibrational axis x .

The heating of a center-of-mass mode grows as the number of trapped ions rises. The use of stretch modes for two-qubit operation in surface traps is preferable [8] since $\dot{n}_{str}/\dot{n}_{com} \propto 100^{-1}$ [26] which is taken into consideration in the next section.

IV. PARALLEL GATES

In sections above we have shown the segmentation of the normal mode frequencies, which gives the ability to perform entangling qubit gates on the segments at parallel. In this section, we demonstrate that Mølmer–Sørensen (MS) gate operation [27] between the

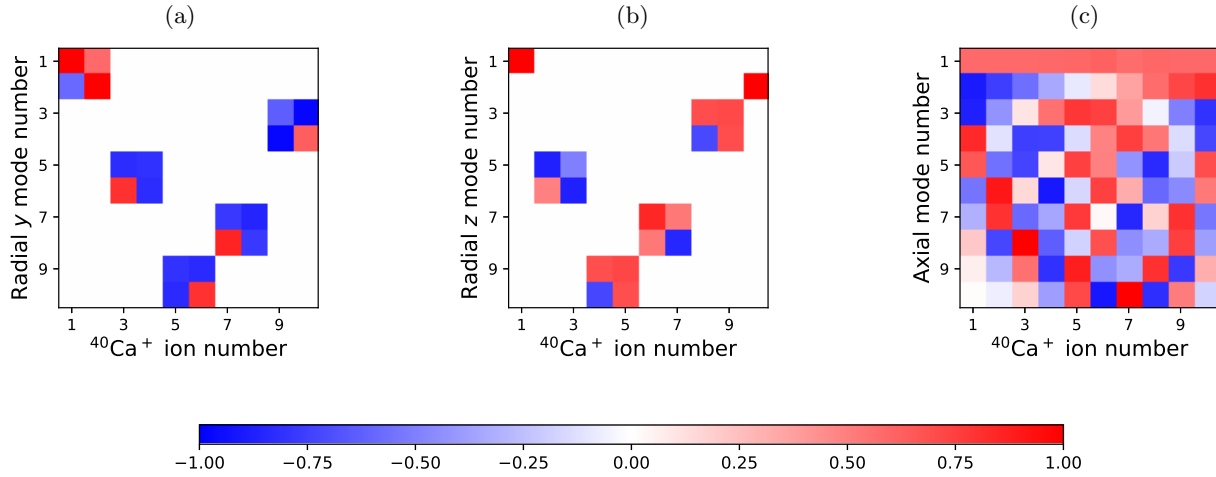


FIG. 6. Mode structure of the nearest neighbor coupling configuration on 10 $^{40}\text{Ca}^+$ ions. (a) Normal mode interaction matrix of y modes. The ion pairs are pinned in parallel. Ions with odd indexes are segmented with left neighbors. c) z normal modes interaction matrix. Ions with odd indices are now segregated with right neighbors, allowing ions to interact solely with their neighbors. d) All-to-all connected axial mode structure. Edge ions can be coupled via the common mode, which interacts with each ion of the crystal.

ions in a segment can be performed with near unit fidelity. Further, we show the pulse sequences necessary to perform unit-fidelity entangling operation on a pair of ions in the segment.

We use the following evolution operator for the MS-gate, which is derived under the rotating wave approximation and in the Lamb-Dicke and resolved-sideband limits [6, 28, 29]:

$$\hat{U}(t) = \exp \left[\sum_{i,m} (\alpha_{i,m}(t) \hat{a}_m^\dagger - \alpha_{i,m}^*(t) \hat{a}_m) \hat{\sigma}_x^{(i)} \right] \times \exp \left[i \sum_{i,j} \chi_{i,j}(t) \hat{\sigma}_x^{(i)} \hat{\sigma}_x^{(j)} \right], \quad (5)$$

where $\hat{\sigma}_x^{(i)}$ is the Pauli- X operator acting on an ion i and $\hat{a}_m^\dagger/\hat{a}_m$ are creation/annihilation operators of mode m . Functions $\alpha_{i,m}(t)$ are responsible for ion-to-mode entanglement, while the phase $\chi_{i,j}$ accounts for entanglement between a pair of qubits i, j .

In general, near-unit fidelity for the ion chains comprised of about dozen of ions can be attained with laser field amplitude modulation as suggested in [6, 28, 29]. The technique requires to divide the gate onto $2N+1$ time intervals with specific constant Rabi frequency Ω_s on each interval for the chain of N ions. In the case of ion chains with spectral division of phonon modes, the MS-gate optimisation can be provided for each ion segment separately. Thus, the length of the chain can be increased without significant loss in MS-gate performance. For each spectral segment one decouples the ions and respective modes and attain a geometric phase of $\chi = \pi/4$

to achieve two-qubit entanglement:

$$\alpha_{i,m}(t_g) = i \sum_{s=1}^{2N+1} \Omega_s \eta_{i,m} \int_{(s-1)t_p}^{st_p} \sin(\mu t) e^{i\omega_m t} dt = 0 \quad (6)$$

$$\chi_{i,j}(t_g) = \sum_{r,s=1}^{2N+1} \Omega_r \Omega_s \Gamma_{rs,ij} = \pi/4, \quad (7)$$

where

$$\Gamma_{rs,ij} = 2 \sum_{m=1}^N \int_{(r-1)t_p}^{rt_p} dt_2 \int_{(s-1)t_p}^{\min(st_p, t_2)} dt_1 \eta_{i,m} \eta_{j,m} \times \sin(\mu t_2) \sin(\mu t_1) \sin[\omega_m(t_2 - t_1)], \quad (8)$$

where Ω_s is the Rabi frequency on a segment s , $t_p = t_g/(2N+1)$ is the segment pulse time, ω_m is the frequency of mode m , $\eta_{i,m} \propto b_{im}$ is the Lamb-Dicke parameter of ion i in the mode m , and $\min(a, b)$ depicts the minimum of two numbers a and b . The control parameters of the gate are detuning μ of a bichromatic field, which is close to the motional mode frequencies, and the gate time t_g .

We consider ions 3 and 4 of the configuration of a chain of 10 $^9\text{Be}^+$ ions depicted on Fig. 5 and the same experimental setup as in [30, 31]. In particular, we use 313.2 nm Raman lasers for gate operation with the 30° angle between the lasers and the trap axis. The time of the gate in the simulations is fixed to $t_g = 200 \mu\text{s}$. Assuming motional independence of the ion segments inside the trap (see configuration in Figure 5 and relation 4), we find optimal Rabi frequencies on intervals for the MS gate for the ions 3 and 4. The results for different laser frequency detunings are shown in Figure 7(a). The absolute value of the Rabi frequency on each time interval does not exceed $2\pi \times 0.22 \text{ MHz}$. In the next section we

calculate the infidelity of the gate induced by the full normal mode spectrum, normal mode frequency drifts and initial non-zero mode temperature.

A. Gate robustness

In surface ion traps one of the leading contributions to gate infidelity comes from the drift of normal modes, which is typically of the order of kHz per several minutes [8]. In a two-qubit operation, drifts of normal modes might lead to an incomplete rupture of spin-motion coupling with normal modes and over-under rotations in the phase space. Using optimal values for in-time segmented Rabi frequencies, we calculate the MS-gate infidelity due to the normal mode drifts in time. We assume linear time dependence of such drifts:

$$\omega_m(t) = \omega_m + \gamma t, \quad (9)$$

where γ is the drift rate which we consider in the range from 100 Hz/min to 1 MHz/min. We set the normal frequencies on each time interval in accordance with formula (9) for fixed drift rates and detuning of the lasers. The

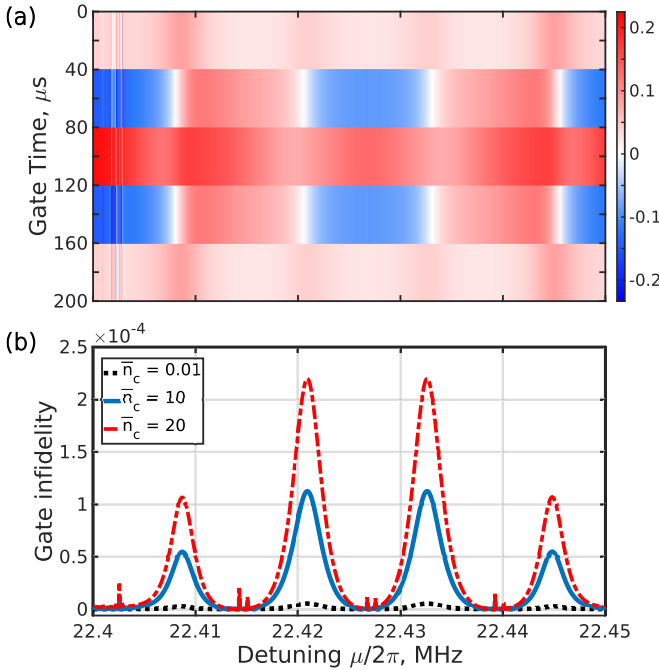


FIG. 7. (a) In-time segmented Rabi frequency in MHz for two neighboring ${}^9\text{Be}^+$ ions. (b) MS-gate infidelity over detuning μ for two neighboring ${}^9\text{Be}^+$ ions for different initial average normal mode occupations. The initial average occupation for ion pair center-of-mass mode is specified in the legend. The drift rates for all the modes are taken as 1 MHz/min. The narrow local infidelity maxima corresponds to the normal frequencies of ions 3 and 4 and half of their sum, all three are repeated with frequency $5/2t_g$ (see the text). Rabi frequency instabilities coincide with gate infidelity local maxima.

overlap of the final state, obtained under the evolution with normal frequency drifts, and ideal states is defined as the fidelity of the entangling phase gate. To calculate the fidelity, we use the analytical formula [29, 32]:

$$\mathcal{F} = \frac{1}{8} [2 + 2(\Gamma_i + \Gamma_j) \cos 2\Delta\chi + \Gamma_+ + \Gamma_-], \quad (10)$$

with $\Delta\chi = \pi/4 - \chi_{i,j}(t_g)$,

$$\begin{aligned} \Gamma_{i,j} &= \exp \left\{ -2 \sum_m |\alpha_{i,j}^m(t_g)|^2 \beta_m \right\}, \\ \Gamma_{\pm} &= \exp \left\{ -2 \sum_m |\alpha_i^m(t_g) \pm \alpha_j^m(t_g)|^2 \beta_m \right\}, \end{aligned} \quad (11)$$

and the factor that accounts for the initial effective normal mode temperature $\beta_m = \coth \frac{\hbar\omega_m}{2k_B T} = \coth \left[\frac{\omega_m}{2\omega_c} \ln \left(1 + \frac{1}{\bar{n}_c} \right) \right]$ with $\bar{n}_c = (e^{\hbar\omega_c/k_B T} - 1)^{-1}$ denoting the average phonon occupation number of the ion pair center-of-mass mode, k_B is the Boltzmann constant. Equation (10) was derived in the assumption of the initial internal state $|\downarrow\downarrow\rangle_z$ of the pair of ions.

To account for the errors coming from the full spectrum of axial normal modes we include all the normal modes and $\alpha_{i,m}(t_g)$ functions in the calculated fidelity. Figure 7(b) shows the results of gate infidelity calculations over the detuning μ for different initial average COM mode occupation number \bar{n}_c . The detuning μ is varied from 22.4 to 22.45 MHz with the step of 2 Hz. Infidelity has narrow maxima for detuning μ close to the normal mode frequencies of the pair and half of their sum, that are repeated after $5/2t_g$ MHz (see Fig. 7(b)). To reach near-unit fidelity, the difference between detuning of the lasers and the local infidelity maxima should be at least 10 Hz. The maximum infidelity for $\bar{n}_c = 20$ reaches $2 \cdot 10^{-4}$ for a drift rate γ of 1 MHz/min and $5 \cdot 10^{-6}$ for drift rates lower than 150 kHz/min. The leading contribution to the infidelity for $\gamma = 1$ MHz/min is the remaining ion-to-mode entanglement, while for drift rates lower than 150 kHz/min the leading contribution comes from the rest of the normal modes of the chain. With the help of considered technique, parallel two-qubit gates on the whole chain can be performed with fidelity greater than 99.9%.

Additionally, we note that multi-loop gates and dynamical decoupling pulse sequences [33, 34] can be used to reduce errors in two-qubit operation.

V. COUPLING ENHANCEMENT

In this section we investigate the capability to increase the coupling between the segments using several ions per trapping site and anharmonic trapping potential. The positive effect of these two aspects have been demonstrated for the two individual wells [15].

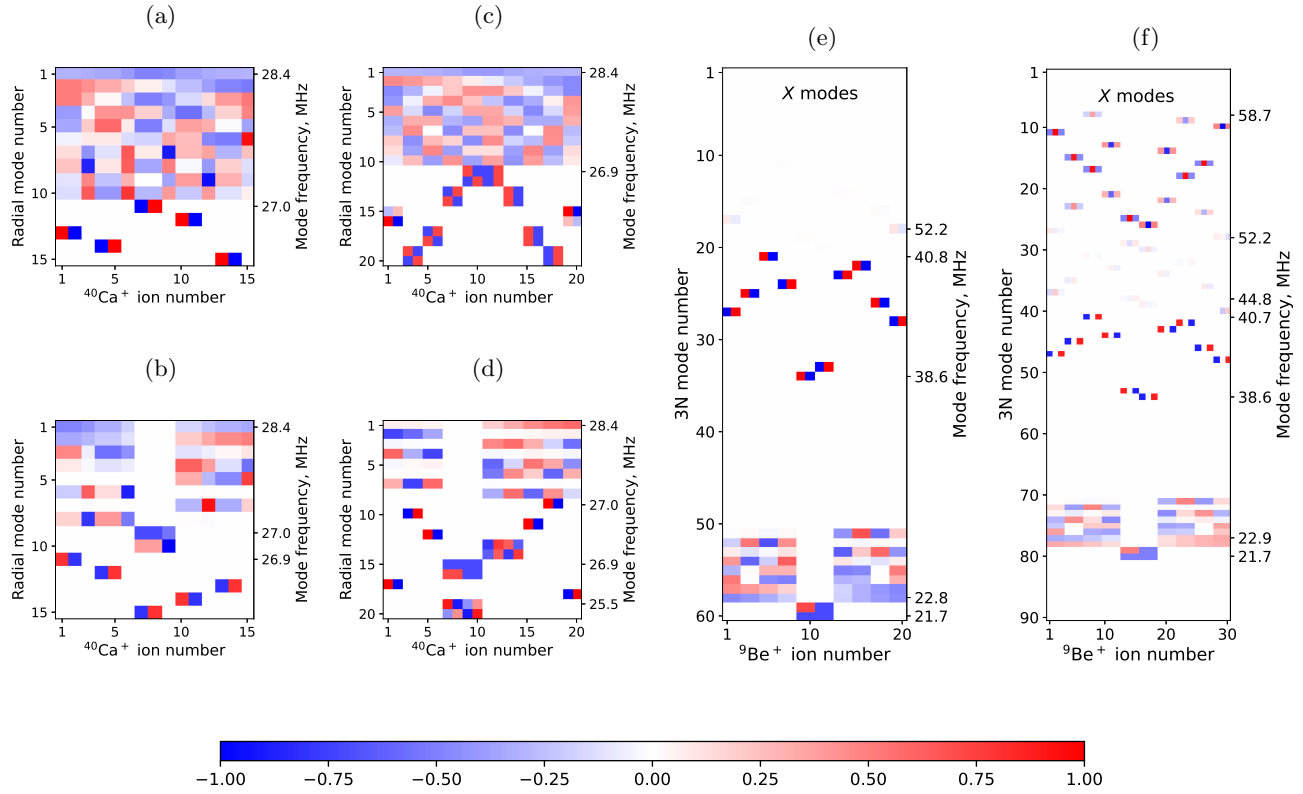


FIG. 8. Radial z (a-d) and x (e-f) normal modes interaction matrices for configurations with each individual trap containing from 1 to 3 ions. On the right y axis of matrix plots a frequency of the mode is presented. (a-b) Interaction matrices for a sequence of repeating single and paired $^{40}\text{Ca}^+$ ions per trap for all-to-all coupling optimization (a) and central traps segmenting (b). (c-d) Configuration with $^{40}\text{Ca}^+$ ion pairs in each trap with all-to-all coupling (c) and segmenting of the traps 4 and 5 (d). (e-f) Pin of 2 central traps for the configuration with 2 (e) and 3 (f) $^{9}\text{Be}^+$ ions in each trap.

First we analyze an impact of the anharmonic terms which becomes visible as ions move further from the potential minimum. Therefore the more ions are trapped in an individual well the more prominent it became. The confinement of several ions per trap is ensured by sufficient trap depth of 100 meV. The linear structure of the resulting crystal is provided by an anisotropy parameter $\alpha = \omega_{\text{axial}}^2/\omega_{\text{radial}}^2$ equals to 0.34 for both $^{40}\text{Ca}^+$ and $^{9}\text{Be}^+$, which is sufficiently low for the linear phase of three ion crystal [35]. A linear alignment of ions in individual traps parallel to the x axis provides the linear form of the whole ion crystal. The resultant ion configuration can be considered as a linear chain. The ion height variation $\delta z_{\text{ion}}/\bar{z} \leq 0.0015$ introduces only third order inaccuracies.

The expansion of the axial trap potential near the minimum in x direction can be expressed as follows [36]:

$$U_{\text{anh}}(\delta x) = \sum_{n=2}^{\infty} \kappa_n \delta x^n \approx \kappa_2 \delta x^2 \left[1 + \left(\frac{\delta x}{\lambda_3} \right) + \left(\frac{\delta x}{\lambda_4} \right)^2 \right],$$

where $l = (Ze/8\pi\epsilon_0\kappa_2)^{1/3}$ – a characteristic length of the potential and $\lambda_n = (\kappa_n/\kappa_2)^{1/(2-n)}$ – anharmonicity scale. For $^{9}\text{Be}^+$ ions in the trap $l = 0.74$ μm ,

$\lambda_3 = 2.4 \times 10^3$ μm and $\lambda_4 = 7.2$ μm . This implies a strong octopole anharmonicity of the trapping potential in each individual well. The coupling strength is determined from the eigenvalues of the Jacobian A_{mn} . The equilibrium positions are determined through simulation, considering an anharmonic form of time-dependent potential. For the dimensionless coordinates $u_n = x_n/l$, the Jacobian takes the following form:

$$A_{mn} = \begin{cases} \frac{\kappa_2^n}{\kappa_2^m} + 6\alpha_n (\delta u_n)^2 + 2 \sum_{\substack{p=1 \\ p \neq n}}^N \frac{1}{|u_n - u_p|^2} & \text{if } n \neq m, \\ \frac{-2}{|u_n - u_m|^2} & \text{if } n = m. \end{cases}$$

Here, $\alpha_n = l^2 \kappa_4^n \kappa_2^o / (\kappa_2^n)^2$ characterizes an octopole anharmonicity of the trap, containing n^{th} ion. κ_2^o is a curvature of the potential in the highest frequency trap.

Normal mode spectrum shown in Figure 8 demonstrates separation on n individual segments, where n – the highest number of ions in an individual trap. For each pair of ions in the same trapping site (Figure 8c-e) the motion is divided into COM and stretch modes. A phonon spectrum, of the whole crystal is then separated into 2 segments, representing ion pairs motion in these

modes. This is a result of the spacing of ions in a single trap being $d_{inner}/d_{outer} = 1/28$ to the distance between two neighbor traps. An ion-ion interaction in a single trap is then $\sim 10^3$ times stronger, then between traps, which dominates the crystal's phonon spectrum. The COM mode segment has the configuration similar to the case with a single ion per trap with doubled mass and charge. Thus, in a harmonic consideration it provides a linear scaling of coupling strength with the ion number per site. The stretch mode case exhibits nontrivial spectrum structure, not applicable for practical tasks due to the reduced spectral separation, typically to 1 Hz.

Another configuration with a single ion in even trapping sites and with two ions in odd sites is demonstrated in Figure 8a-b. The pinned pair of traps indicates the coupling of one ion and an ion pair in COM mode. The fact, that coupling still occurs between the traps with different number of ions simplifies the experiment by allowing an unequal number of particles in each trap. A configuration of $^{40}\text{Ca}^+$ ion pairs in each trap is presented in Figure 8c-d. The ion pairs in stretch mode demonstrate low coupling strength $\Omega_I = 1$ Hz, so the operations should be performed with COM mode of ions. No anharmonic frequency shifts are provided for $^{40}\text{Ca}^+$ ions because a coupling is achieved on radial modes. The ions are distributed along x axis, and their position along x axis does not change.

Figure 8e-f demonstrates the axial mode configuration of $^9\text{Be}^+$ ion pairs and triplets with two central traps pinned. Although there is no coupling between x and y normal modes due to the high difference between mode frequencies in individual traps the phonon spectrum is represented through the 3N interaction matrix. The calculated coupling between ions in pinned traps is represented in Table I.

Mode interaction matrix for a 2-ion configuration from the Figure 8e in the presence of anharmonic effects is

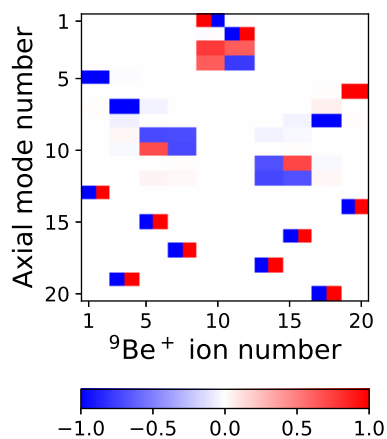


FIG. 9. An uncoupled interaction matrix of Figure 8e configuration in the presence of octopole anharmonicity.

demonstrated in Figure 9. The central traps are still in resonance, since the anharmonic parameters $\alpha_{central}$ are equal due to the central symmetry of the structure. However, the anharmonicity varies in the range of $\alpha \sim [-0.014, -0.021]$ with the trap number. As a result, numerous ions per trap configuration experience harmonic resonance detuning.

Overall we demonstrate a linear increase in coupling strength between traps, by loading more ions per each trapping site. However, the anharmonic shifts of secular frequencies decouple the non-symmetrical individual wells. An additional minimization of the variance in the 4th order potential expansion is needed to compensate this effect. The compensation can be performed by additional optimization using the side DC voltages.

VI. CONCLUSION AND OUTLOOK

In conclusion, we described and characterized a new surface trap design allowing to connect or disconnect the distant sites of the trap through coulomb interaction. In particular, we demonstrated that by changing the DC voltages on the trapping electrodes we can unite the chosen ions into pairs with unique phonon mode frequencies. For this we modeled the trapping potential and the corresponding phonon mode spectra for calcium and beryllium ions. The proposed trap design was tested for single ions in each trapping site and for the two ions in a site, but, in general, each segment can be comprised of any reasonable number of ions. We also analyzed how the obtained results change with the trap anharmonicity. The second part of the paper focused on the performance of the parallel MS-gate operation for the segmented ion chains. We maximize the fidelity of the gates by dividing the time of the MS-gate pulse into 5 intervals. The infidelity of the gate was calculated under the drift of the normal mode frequencies expected in experiment and for different initial normal mode temperatures. We show that for experimental drift rates of few kHz per several minutes the infidelity from the normal frequencies drift does not exceed $5 \cdot 10^{-6}$ if the detuning is not in the resonance with normal mode frequencies of the ion pair. For higher drift rates the ion-to-mode entanglement starts to play an important role. Namely, we obtained the fidelity of the gate of 99.97% for a drift rate $\gamma = 1$ MHz/min and initial average COM mode occupation number $\bar{n}_c = 20$.

Overall, the proposed design can indeed become a powerful tool to connect distant surface traps. Here we

TABLE I. Coupling strength Ω_I/π in spectral segments from configurations on Fig. 8e-f. The normal frequencies are calculated in both harmonic and anharmonic potential model.

Potential	$^9\text{Be}^+$ pairs	$^9\text{Be}^+$ triplets
Harmonic	3039 Hz	4589 Hz
Anharmonic	3208 Hz	4998 Hz

mostly focused on the gate based approach of quantum computation. But in general the trap can be also utilized for quantum simulations. We are expecting the proposed design to be competitive with the present scaling methods in respect of achieving large-scale QC.

ACKNOWLEDGEMENTS

This work was supported by Rosatom in the framework of the Roadmap for Quantum computing (Contract No. 868-1.3-15/15-2021 dated October 5).

Appendix A: Ion dynamics simulation

According to the concept of superposition the total potential above the electrodes can be obtained by adding the potential generated by each electrode. LAMMPS software is used to perform the simulation of ion motion [37]. The molecular dynamics approach numerically integrates via the Verlet algorithm Newton's classical equations of motion of each confined atom to describe the motions of large systems with many particles [38]. Laser cooling of ions and background gas collisions are described with Langevin equation:

$$m_i \frac{d^2 \mathbf{x}}{dt^2} = F_i(\mathbf{x}) - \gamma_i \dot{\mathbf{x}} + f_i(t), \quad (\text{A1})$$

for ions with mass m_i , confined in the potential force F_i , under the laser cooling force with strength γ_i and stochastic force f_i .

The following resultant potential is used to determine the force F_i .

$$U_{pot}(x, y, z, t) = \sum_{i=1}^{N_{DC}} \phi_{DC}^i(x, y, z) + \sum_{i=1}^{N_{RF}} \phi_{RF}^i(x, y, z) \cos(\Omega_{RF} t) + \sum_{n=1}^N \sum_{m>n}^N \frac{Z^2 e^2}{4\pi\epsilon_0} \frac{1}{|\vec{r}_n - \vec{r}_m|^2}, \quad (\text{A2})$$

for N ions confined in the trap with N_{DC} , N_{RF} – number of DC and RF electrodes correspondingly.

The analytical form [24] of the field produced by a rectangular surface electrode under unit voltage is taken into consideration in the modeling of the electric field above the plane of the electrodes and subsequent calculation of the equilibrium positions:

$$\begin{aligned} \phi(x, y, z) = & \frac{V}{2\pi} \left[\tan^{-1} \left(\frac{(x_b - x)(y_b - y)}{z\sqrt{z^2 + (x_b - x)^2 + (y_b - y)^2}} \right) \right. \\ & - \tan^{-1} \left(\frac{(x_a - x)(y_b - y)}{z\sqrt{z^2 + (x_a - x)^2 + (y_b - y)^2}} \right) \\ & - \tan^{-1} \left(\frac{(x_b - x)(y_a - y)}{z\sqrt{z^2 + (x_b - x)^2 + (y_a - y)^2}} \right) \\ & \left. + \tan^{-1} \left(\frac{(x_a - x)(y_a - y)}{z\sqrt{z^2 + (x_a - x)^2 + (y_a - y)^2}} \right) \right], \end{aligned} \quad (\text{A3})$$

where V is the applied voltage and $(x_a, y_a, 0)$ and $(x_b, y_b, 0)$ are the coordinates of two opposing vertices of the planar electrode. The analytic form of potential from the trap is merged with the pyLion package [39] to perform the simulation of trapped ions.

Appendix B: DC voltage set optimization

Due to the cross influence of DC electrodes on neighboring ions an optimization procedure for the entire set of voltages is required. The maximum allowable voltage of 6 V causes a (12.3, 9.4, 19.2)% and (11.6, 8.9, 18.1)% alteration in the secular frequency $(\omega_x, \omega_y, \omega_z)$ of Be and Ca ions correspondingly. Radial secular frequencies are least affected by crosstalk suffered by the near proximity of the central DC electrodes. The secular frequencies of calcium and beryllium ions shift to (2.4, 0.2, 0.4)% and (2.3, 0.2, 0.4)% at zero center and 6 V outer DC electrodes, respectively. Long ion-ion distances put a strict condition on the secular frequency matching, necessary for the resonance. The Adam algorithm for optimization is used [40]. Mode configuration is obtained with the loss function as a quadratic norm of difference between the desired and calculated frequency sets. The calculation of the secular frequency in each pit requires self-optimization to achieve a minimum of pseudopotential in the capture position, which increases the time of each iteration of gradient descent. The z principal axis secular frequencies of 10 individual potential wells are set for the proof-of-principle investigation due to their minimal cross-talk and large range of achievable values (Figure 4). Improving x secular frequencies is more demanding due to an increased cross-talk on axial modes. The voltage configuration in Figure 5 was obtained by guessing a good starting point, performed by hand. The edge DC electrodes are used to lower the DC voltages on trapping sites.

[1] J. I. Cirac and P. Zoller, *Nature* **404**, 579–581 (2000).

[2] David P. DiVincenzo, *Fortschritte der Physik* **48**, 771–783 (2000).

[3] T. P. Harty *et al.*, *Phys. Rev. Lett.* **113**, 220501 (2014).

[4] C. J. Ballance *et al.*, *Phys. Rev. Lett.* **117**, 060504 (2016).

[5] Colin D. Bruzewicz *et al.*, *Applied Physics Reviews* **6**, 021314 (2019), <https://doi.org/10.1063/1.5088164>.

[6] K. Sosnova *et al.*, *Phys. Rev. A* **103**, 012610 (2021).

[7] D. Kielpinski *et al.*, *Nature* **417**, 709–711 (2002).

[8] K. K. Mehta *et al.*, *Nature* **586**, 533–537 (2020).

[9] C. R. Craig *et al.*, *Phys. Rev. Lett.* **127**, 130505 (2021).

[10] R. Srinivas *et al.*, *Nature* **597**, 209–213 (2021).

[11] N. Daniilidis *et al.*, *Journal of Physics B: Atomic, Molecular and Optical Physics* **42**, 150412c (2009), 749–752 (2005).

[12] D. An *et al.*, *Phys. Rev. Lett.* **128**, 063201 (2022).

[13] F. Hakelberg *et al.*, *Phys. Rev. Lett.* **123**, 100504 (2019).

[14] K. Brown *et al.*, *Nature* **471**, 196–199 (2011).

[15] M. Harlander *et al.*, *Nature* **471**, 200–203 (2011).

[16] A. Wilson *et al.*, *Nature* **512**, 57–60 (2014).

[17] Jonathan P. Home, “Quantum science and metrology with mixed states,” *Quantum science and metrology with mixed states* (2013).

[18] Roman Schmied *et al.*, *Phys. Rev. Lett.* **102**, 233002 (2009).

[19] S. Narayanan *et al.*, *Journal of Applied Physics* **110**, 114909 (2011), <https://doi.org/10.1063/1.3665647>.

[20] F. A. Shaikh and A. Ozakin, *Journal of Applied Physics* **112**, 074904 (2012).

[21] C. F. Roos *et al.*, *Phys. Rev. A* **77**, 040302 (2008).

[22] P. Holz, Ph.D. thesis, University of Innsbruck (2020).

[23] P. C. Souers *et al.*, Tech. Rep. (1977) uCRL-52226.

[24] M. G. House, *Phys. Rev. A* **78**, 033402 (2008).

[25] D. F. V. James, *Applied Physics B* **66**, 181–190 (1998).

[26] M. Malinowski, Ph.D. thesis, ETH Zurich (2021).

[27] K. Mølmer and A. Sørensen, *Phys. Rev. Lett.* **82**, 1835–1838 (1999).

[28] T. Choi *et al.*, *Phys. Rev. Lett.* **112**, 190502 (2014).

[29] S.-L. Zhu *et al.*, *Phys. Rev. Lett.* **97**, 050505 (2006).

[30] D. Leibfried *et al.*, *Nature* **422**, 412–415 (2003).

[31] M. Marinelli, Ph.D. thesis, ETH Zurich (2020).

[32] C.M Figatt, Ph.D. thesis, University of Maryland (2018).

[33] A. R. Milne *et al.*, *Phys. Rev. Applied* **13**, 024022 (2020).

[34] D. Hayes *et al.*, *Phys. Rev. Lett.* **109**, 020503 (2012).

[35] L. L. Yan *et al.*, *Scientific Reports* **6**, 21547 (2016).

[36] J. P. Home *et al.*, *New Journal of Physics* **13**, 073026 (2011).

[37] E. Bentive *et al.*, *Computer Physics Communications* **253**, 107287 (2020).

[38] William C. Swope *et al.*, *The Journal of Chemical Physics* **76**, 637–649 (1982), <https://doi.org/10.1063/1.442716>.

[39] E. Bentive *et al.*, *Computer Physics Communications* **253**, 107287 (2020).

[40] D. P. Kingma and J. Ba, “Adam: A method for stochastic optimization,” (2014).

[41] Seth Lloyd, *Science* **273**, 1073–1078 (1996), <https://www.science.org/doi/pdf/10.1126/science.273.5278.1073>.

[42] Richard P. Feynman, *Int J Theor Phys* **21**, 467–488 (1982).

[43] Iulia Buluta and Franco Nori, *Science* **326**, 108–111 (2009), <https://www.science.org/doi/pdf/10.1126/science.1177838>.

[44] R Schmied *et al.*, *New Journal of Physics* **10**, 045017 (2008).

[45] J. Chiaverini *et al.*, *Phys. Rev. A* **77**, 022324 (2008).

[46] P. Hou *et al.*, (2022), arXiv:2205.14841.

[47] D. J. Heinzen and D. J. Wineland, *Phys. Rev. A* **42**, 2977–2994 (1990).

[48] *Optical Physics* **42**, l.150412c (2009), 749–752 (2005).

[49] T. Rosenband *et al.*, *Science* **319**, 1808–1812 (2008).

[50] OP de Sá Neto *et al.*, *Scientific Reports* **12**, 1–15 (2022).

[51] K. Lakhmanskiy *et al.*, *Phys. Rev. A* **99**, 023405 (2019).

[52] Ch Schneider, Diego Porras, and Tobias Schaetz, *Reports on Progress in Physics* **75**, 024401 (2012).

[53] M. Horjant *et al.*, *Phys. Rev. X* **11**, 041033 (2021).

[54] C. D. Bruzewicz *et al.*, *Nature communications* **7**, 1–6 (2016).

[55] J. M. Sage *et al.*, *Phys. Rev. A* **86**, 013417 (2012).

[56] M. Pino *et al.*, *Nature* **592**, 209–213 (2021).

[57] W. K. Hensinger, “Quantum computer based on shuttling trapped ions,” (2021).

[58] R. B. Blakestad *et al.*, *Phys. Rev. Lett.* **102**, 153002 (2009).

[59] Tobias Olsacher *et al.*, *PRX Quantum* **1**, 020316 (2020).

[60] C. Monroe *et al.*, *Phys. Rev. A* **89**, 022317 (2014).

[61] B. B. Blinov *et al.*, *Nature* **428**, 153–157 (2004).

[62] P. Maunz *et al.*, *Nature Physics* **3**, 538–541 (2007).

[63] D. L. Moehring *et al.*, *Nature* **449**, 68–71 (2007).

[64] J. P. Home, in *Advances in Atomic, Molecular, and Optical Physics*, Vol. 62 (2013) pp. 231–277.

[65] M. Brownnutt *et al.*, *Rev. Mod. Phys.* **87**, 1419–1482 (2015).

[66] M. W. van Mourik *et al.*, *Phys. Rev. A* **105**, 033101 (2022).

[67] M. K. Joshi *et al.*, *New Journal of Physics* **22**, 103013 (2020).

[68] A. Mohammadi *et al.*, *Applied Physics B* **125**, 122 (2019).

[69] R. Blümel *et al.*, *Phys. Rev. A* **40**, 808–823 (1989).

[70] S. Narayanan *et al.*, *Journal of Applied Physics* **110**, 114909 (2011).

[71] C. J. Ballance, Ph.D. thesis, University of Oxford (2014).

[72] R. Schmied *et al.*, *New Journal of Physics* **12**, 023038 (2010).

[73] X. Rebecca Nie *et al.*, *Physics Letters A* **373**, 422–425 (2009).

[74] D. J. Gorman *et al.*, *Phys. Rev. A* **89**, 062332 (2014).

[75] S. Narayanan *et al.*, *Journal of Applied Physics* **110**, 114909 (2011).

[76] D. J. Gorman *et al.*, *Phys. Rev. Lett.* **119**, 193602 (2017).

[77] R. Blümel *et al.*, *npj Quantum Information* **7**, 147 (2021).